The frost restraining effect of solar air collector applied to air source heat pump

Yan Jiang [a,1], Jiaxuan Pu [a, 1], Huan Zhang [a, b], Sujie Liu [a], Yaran Wang [a, b, *], Shijun You [a, b], Zhihao Wan [a], Zhangxiang Wu [a], Xianwang Fan [a], Zhikai Liu [a], Shen Wei [c]

[a] School of Environmental Science and Engineering, Tianjin University, Tianjin,300350, PR China

[b] Key Laboratory of Efficient Utilization of Low and Medium Grade Energy (Tianjin University), Ministry of Education of China, Tianjin 300350, PR China

[c] The Bartlett School of Construction and Project Management, University College London (UCL), 1-19 Torrington Place, London WC1E 7HB, United Kingdom

Abstract

The air source heat pump has been demonstrated to be an efficient clean space heating technology, but the frosting on the exterior surface of the evaporator will largely decrease its performance. In this paper, the triangular solar air collector is adopted for evaporator frost restraint of the air source heat pump, and the dynamic heat transfer model of the triangular solar air collector and quasi-steady-state frosting model of the evaporator were established and coupled. The effect of frost layer thickness variation on evaporator air flow is considered based on the resistance factor to improve the applicability of the model. The heat flux and water vapor diffusion flux at different frost time and frost thickness were calculated, and the frosting characteristics of the air source heat pump with the triangular solar air collector and the conventional air source heat pump were compared on varying

[*] *Corresponding author. Tel.: +8602227892626; fax: +8602227892626.*
E-mail addresses: yaran_wang@tju.edu.cn.

[1] *These authors contributed equally to this work.*

working conditions and typical daily meteorological parameters. Results show that triangular solar air collector can effectively restrain the frosting of the air source heat pump, and when the solar irradiance is 500 W/m^2, the triangular solar air collector can reduce the frost thickness by more than 15%. The triangular solar air collector increases the total heat flux by 101.4 W/m^2 under frosting conditions, which reduces half of the defrosting times and increases the heat exchange of the evaporator by 36.6 % during a typical day, indicating that triangular solar air collector significantly improved the energy efficiency of air source heat pump on frosting condition.

Keywords

Air source heat pump; Frost resistance; Solar air collector; Heat transfer model

Nomenclature

A	surface area (m^2)	T	temperature (K)
A_{total}	total heat transfer area of finned-tube evaporator (m^2)	T_{sft}	equivalent temperature of the evaporator surface (K)
A_{tube}	tube base area of the finned-tube evaporator (m^2)	$\overline{T}_{\mathrm{a}}$	average temperature of the incoming air (K)
C	absorption coefficient of water by frost layer (-)		
C_1	evaporator fan similar law formula constant (-)	u	velocity in the x direction (m/s)
c_p	specific heat capacitance (J/(kg·K))	V	volume (m^3)
D_{eff}	effective water diffusion coefficient (m^2/s)	v	velocity in the y direction (m/s)
D_{std}	standard water diffusion coefficient (m^2/s)	w	moisture content (g/kg)
d	thickness (m)	w_{fs}	saturated air moisture content corresponding to the frost surface temperature (g/kg)
d_3	fin root diameter of evaporator (m)		
E_{T}	residual tolerance (-)		
f	resistance factor (-)	$\overline{w}_{\mathrm{a}}$	average moisture content of incoming air (g/kg)
h_{eff}	convective heat transfer coefficient (W/(m^2·K))		
$h_{\mathrm{m,eff}}$	convective mass transfer coefficient (m/s)	**Subscript**	
I	solar irradiance (W/m^2)	a	air
i_{sv}	vaporization latent heat of water (kJ/kg)	ab	absorb
j_{N}	j factor of N-row-tube finned-tube evaporator (-)	air	air
k_{f}	thermal conductivity of the frost (W/(m·k))	conv	convection

L	fin length along the airflow direction (m)	env	environment
M	mass (kg)	f	frost
M_a	mass transfer of water vapor between incoming air	fin	fin
	and frost layer (g/(m^2·s))	fs	frost surface
N_f	fan speed (r/min)	hole	hole
m	mass flow rate (kg/s)	ho	housing
m_{fs}	mass flux of water vapor between incoming air and	i	ice
	frost layer (g/(m^2·s))	in	inlet
m_ρ	water mass flux for increasing the frost density	out	outlet
	(g/(m^2·s))	rad	radiation
m_δ	water mass flux for thickening the frost layer	sat	saturated
	(g/(m^2·s))	sens	sensible heat
P	porosity factor (-)	tcp	transparent cover plate
p_e	full pressure (Pa)	tube	tube base
Q	heat transfer capacity (W)	**Greek symbols**	
q	heat flux (W/m^2)	μ	dynamic viscosity (kg/m·s)
q_{conv}	convective heat transfer (W)	τ	time (s)
q_{rad}	radiant heat transfer (W)	λ	thermal conductivity (W/m·K)
s	fin pitch of finned-tube evaporator (m)	δ	thickness (m)
s_b	beam solar irradiance absorbed (W)	ρ	density (kg/m^3)
s_d	diffusion solar irradiance absorbed (W)	v	kinematic viscosity (m^2/s)

1 Introduction

Renewable space heating technologies are potential solutions for decarbonization [1]. Air source heat pumps (ASHPs) are widely used in space heating due to their advantages of availability of renewable energy [2], high energy efficiency, reliable operation [3], and limited space occupation [4]. But under specific ambient temperatures and high humidity, frost will form on the exterior surface of the outdoor evaporator of ASHP [5], which will deteriorate the heat transfer and decrease the performance of ASHP [6]. Research shows that frosting will reduce the energy efficiency of the ASHP by 40 % and the heating capacity by 43 % [7].

In order to understand the frosting phenomenon and alleviate its adverse influences on ASHP performances, numerical and experimental investigations on frosting mechanisms and frost characteristics have been carried out. Song et al. [8] considered that the thickness of the frost layer is the most significant parameter in the frosting process of ASHP because of its direct effects on the airflow through the evaporator. Zhang et al. [9] developed a novel frost model considering the variation of frost density along the frost thickness direction, which can improve the prediction precision of frost thickness by 5.1 %. The experiment showed that the frost densities on the surface of the frost layer and the surface of the finned-tube evaporator can differ by 68 % [10]. The external environmental parameters are the main factors affecting frosting on the outdoor evaporator. Seker et al. [11] established a transient semi-empirical model of frost formation on the finned-tube evaporator and analyzed the effects of air temperature, relative humidity and the surface temperature of the evaporator on the growth rate of frost thickness. Ji et al. [12] analyzed the influence of relative humidity on the frosting of the finned-tube solar-assisted heat pump (SAHP). They found that the COP of finned-tube SAHP decreases by 11% when the relative humidity of the incoming air increases from 50% to 70%.

Due to the negative effects of frosting on the ASHPs, it is necessary to investigate methods to restrain frosting [13]. Current research and applications of ASHP restrain frosting through three main avenues [14]: (1) Restraining frost with additional equipment; (2) Optimizing the structure of outdoor evaporators; (3) Changing inlet air parameters of evaporators. Tan et al. [15] and Sonobe et al. [16] applied ultrasonic vibration and air-jet to ASHP, which can restrain frost effectively but increase the initial investment. Lee et al. [17] analyzed the air-side heat transfer characteristics of flat plate finned-tube evaporators at different structures under frosting conditions, showing that fin pitches and staggered tube alignment had a great effect on frost restraining, but changing the structure of the evaporator may decrease its heat transfer performance under non-frosting condition. Compared to the above methods, changing the inlet air parameters of evaporators is an effective and easily-attainable way to restrain frost and does not require changes to the marketed evaporator structure. And a more feasible and ecological approach is to utilize solar thermal energy. Huang et al. [18] established a dynamic model of frosting in a flat-plate direct-expansion solar-assisted heat pump (DX-SAHP) and analyzed its frosting conditions. Results showed that when the ambient temperature was -1℃ and the relative humidity was 70%, the solar radiation increased from 0 W/m^2 to 100 W/m^2, and the thickness of the frost layer decreased from 0.176 mm to 0 mm. According to Kong et al. [19], higher solar radiation could effectively increase the evaporation temperature of the SAHP collector/evaporator and result in a decrease in the frosting rate.

Solar air collectors (SACs) are also extensively applied as a renewable energy space heating method [20], and can be coupled with ASHP to enhance both performance [21]. The SAC-coupled ASHP can preheat the evaporator inlet air, thus increasing the evaporation temperature and the COP of the ASHP [22]. However, the frost restraining effect it plays in this process has been ignored by researchers and rarely analyzed.

In this paper, a novel triangular solar air collector (TSAC) is proposed and coupled with ASHP to provide a frost restraint effect. A dynamic heat transfer model of the novel TSAC and a quasi-steady-state frost model are developed and verified by experiment. The relationship between airflow and resistance factor is considered in the frost model in order to be quickly adjusted to different evaporators. Based on the models, the frost characteristics of the ASHP with the novel TSAC are compared with the conventional ASHP under different operating conditions, and the effectiveness of the TSAC for frost restraint was analyzed.

The main contributions of this study can be summarized as: (1) A novel coupled frost model for the TSAC and ASHP evaporator was established with better applicability. (2) The frosting characteristics of the finned-tube evaporator were investigated numerically. (3) The effectiveness of TSAC in restraining frost was studied.

2 Model development and solution

2.1 The model of triangular solar air collector

2.1.1 The physical model of triangular solar air collector

The structure of the proposed TSAC is shown in Fig 1. The TSAC places facing south and the tilted transparent cover plate is inclined at 60°. The recirculating air is extracted by the fan into the TSAC from the air inlet, exchanges heat with the solar-heated perforated corrugated absorbers (PCAs), and then leaves from the outlet. The PCAs are installed in three parts inside the TSAC, at angles of 30°, 120° and 52°, to absorb solar irradiance and heat the circulating air without blocking each other throughout the heating season. The porosity factor of PCAs is 0.085 and the pore size is 4mm. The corrugated shape and porous structure of PCAs can break the air boundary layer on their surface, thus enhancing turbulence and strengthening heat transfer. The absorption rate of PCAs reaches 0.92 with black chromium coating. The sides, backs and undersides of the TSAC are coated with insulation material. The geometric and physical parameters of the TSAC are listed in Table 1.

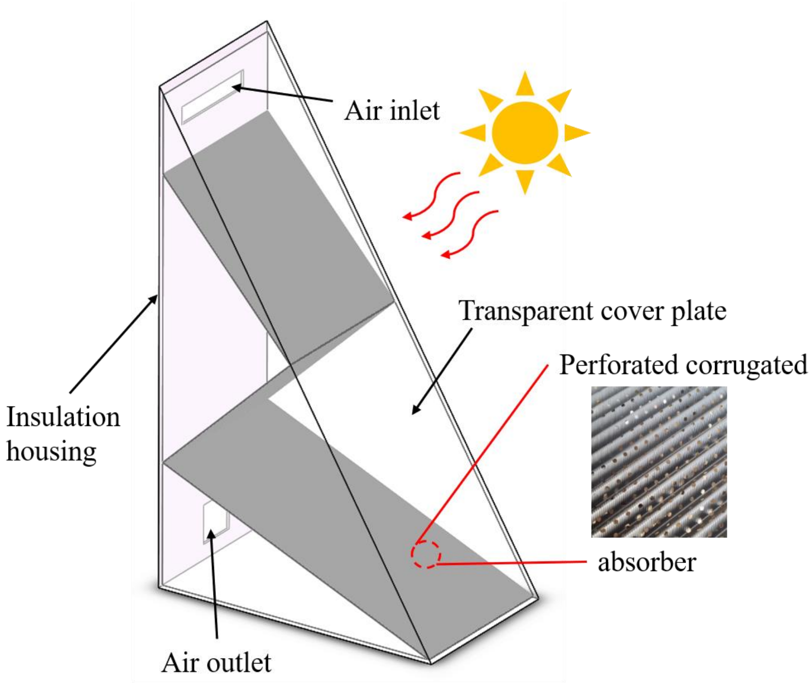

Fig. 1. Structure of the TSAC

Table 1. The geometric and physical parameters of the TSAC

TSAC	Section size: 2.4×2.1×1.2 (m×m×m), width: 0.7 (m)
Single/Double transparent cover plate	Materials: Polycarbonate; Physical parameter: α_{tcp}=0.1; ε_{tcp}=0.67

Perforated corrugated	λ_{tcp}=0.2/0.06 (W/(m·K)); τ_{tcp}=0.89/0.79;
absorber	Physical parameter: λ_{ab}=14.8 (W/(m·K)); α_{ab}=0.92; ε_{ab}=0.2;
Insulation housing	Materials: Polystyrene board and galvanized sheet
	Physical parameter: λ_{ho}=0.028 (W/(m·K)); α_{ho}=0.2; ε_{ho}=0.1
Air inlet/outlet	Section size: 0.15×0.4/0.2×0.2 (m×m), length: 0.6 (m)

The following assumptions are considered to establish the mathematical model of the TSAC:

(1) The heat transfer of the TSAC in the cross-section is neglected.

(2) The velocity of the recirculating air is uniformly distributed over the TSAC cross sections.

(3) The density of recirculating air is considered constant as the air inside the TSAC has a narrow range of temperature and pressure variations.

(4) The thermal parameters of the insulation housing, PCA, transparent cover plate and recirculating air are temperature independent.

(5) The heat losses between the insulation housing and the external environment are ignored.

2.1.2 The mathematical model of triangular solar air collector

A one-dimensional heat transfer model of the TSAC was developed along the elevation direction. The energy conservation equation for the recirculating air is formulated as Eq. (1). It consists of the heat unsteady term, the convection term, and source terms representing the convective heat exchange between the recirculating air and TSAC components.

$$M_{\mathrm{air}} c_{\mathrm{p,air}} \frac{\partial T_{\mathrm{air}}}{\partial \tau} + M_{\mathrm{air}} c_{\mathrm{p,air}} \frac{\partial (u_{\mathrm{air}} T_{\mathrm{air}})}{\partial x} = q_{\mathrm{conv,ho\text{-}air}} + q_{\mathrm{conv,hole}} + q_{\mathrm{conv,tcp\text{-}air}} + q_{\mathrm{conv,ab\text{-}air}} \quad (1)$$

Energy conservation equations for the transparent cover plates, Eq. (2), the PCA, Eq.

(3) and the insulated housing, Eq. (4) are formulated as follows. Their composition is similar to Eq. (1), but without the convection term, possessing the diffusion term and radiative heat gain denoted by source terms. More detailed descriptions of the TSAC model are in our previous published work [23].

$$M_{\mathrm{tcp}} c_{\mathrm{p.tcp}} \frac{\partial T_{\mathrm{tcp}}}{\partial \tau} = V_{\mathrm{tcp}} \lambda_{\mathrm{tcp}} \frac{\partial^2 T_{\mathrm{tcp}}}{\partial x^2} + s_{\mathrm{b.tcp}} + s_{\mathrm{d.tcp}} + q_{\mathrm{conv.tcp\text{-}env}} + q_{\mathrm{conv.tcp\text{-}air}} + q_{\mathrm{rad.tcp\text{-}env}} + q_{\mathrm{rad.tcp\text{-}ab}} + q_{\mathrm{rad.tcp\text{-}ho}} \quad (2)$$

$$M_{\mathrm{ab}} c_{\mathrm{p,ab}} \frac{\partial T_{\mathrm{ab}}}{\partial \tau} = V_{\mathrm{ab}} \lambda_{\mathrm{ab}} \frac{\partial^2 T_{\mathrm{ab}}}{\partial x^2} + s_{\mathrm{b,ab}} + s_{\mathrm{d,ab}} + q_{\mathrm{conv,ab\text{-}air}} + q_{\mathrm{conv,hole}} + q_{\mathrm{rad,ab\text{-}tcp}} + q_{\mathrm{rad,ab\text{-}ho}} + q_{\mathrm{rad,ab\text{-}ab}} \quad (3)$$

$$M_{\mathrm{ho}} c_{\mathrm{p,ho}} \frac{\partial T_{\mathrm{ho}}}{\partial \tau} = V_{\mathrm{ho}} \lambda_{\mathrm{ho}} \frac{\partial^2 T_{\mathrm{ho}}}{\partial x^2} + q_{\mathrm{conv,ho\text{-}air}} + q_{\mathrm{rad,ho\text{-}tcp}} + q_{\mathrm{rad,ho\text{-}ab}} + q_{\mathrm{rad,ho\text{-}ho}} \quad (4)$$

The discrete diffusion, convective, and unsteady terms were represented by the central difference, first-order upwind, and fourth-order Runge-Kutta methods, respectively.

2.1.3 The boundary and initial conditions

The boundary conditions of the mathematical TSAC model are:

$$T_{\mathrm{air}}(x,\tau)\big|_{x=0} = T_{\mathrm{in}}(\tau)$$

$$m_{\mathrm{air}}(x,\tau)\big|_{x=0} = m_{\mathrm{in}}(\tau)$$

The variations of environmental temperature T_{env}, wind speed v_{env}, and solar irradiance I_{g} with time are considered. The initial conditions of the mathematical model are listed below:

$$T_{\mathrm{air}}(x,\tau)\big|_{\tau=0} = T_{\mathrm{tcp}}(x,\tau)\big|_{\tau=0} = T_{\mathrm{ab}}(x,\tau)\big|_{\tau=0} = T_{\mathrm{ho}}(x,\tau)\big|_{\tau=0} = T_{\mathrm{env}}\big|_{\tau=0}$$

2.2 Frosting model

A quasi-steady-state frosting model of the finned-tube evaporator has been developed and coupled with the mathematical model of the TSAC. The following assumptions are considered to simplify the frosting model and facilitate the calculation:

2.2.1 Assumptions of the frosting model

(1) The frost thickness is considered constant during a time step and only updated at the end of the time step.

(2) The heat capacity of the frost layer is ignored.

(3) Only the heat and mass transfer along the thickness direction of the frost layer is considered in the one-dimensional frosting model.

(4) The original growth period during frosting is not considered, i.e., the initial frost thickness and frost density are directly input.

(5) The thickness of frost is consistent across the effective frosting area of the finned-tube evaporator.

(6) The water content of the air inside the frost layer is supersaturated, and the amount of water absorbed inside the frost layer is proportional to the density difference between the supersaturated water inside the frost layer and the saturated water at the corresponding frost layer temperature.

(7) The thermal conductivity of the frost is determined only by the frost density.

(8) The convective heat and mass transfer inside the frost layer are ignored.

2.2.2 The mathematical model of frosting

To simplify the frost model, the frost distribution is assumed to be the same for each heat transfer unit of the finned-tube evaporator. As shown in Fig. 2, a heat and mass transfer unit consists of fins in a box and copper tubes on both sides of the fins, which are frosted on the windward side. The heat and mass transfer processes of the frosting on the finned-tube evaporator are shown in Fig. 3. Heat conduction exists between the frost layer and the evaporator surface. Heat and mass transfer occur inside the frost layer through thermal conduction and molecular diffusion. The incoming air flows over the frost layer and exchanges heat and mass with it convectively. For the steam entering the frost layer through convective mass transfer, part of it condenses on the surface thickening the frost layer, and the rest is absorbed into the interior of the frost layer increasing its density.

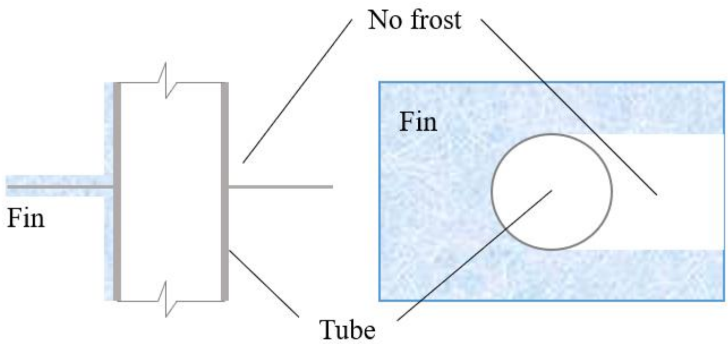

Fig. 2. The frost distribution of a heat transfer unit

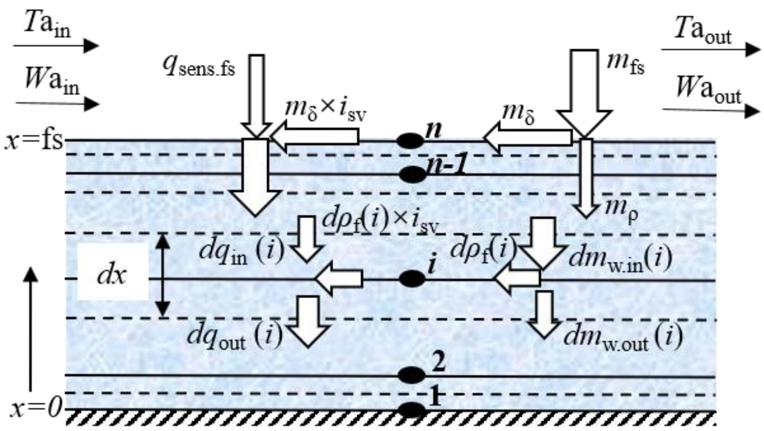

Fig. 3. The heat and mass transfer processes of frosting

The frost model employs the external node method and the control body is divided along the frost thickness direction. The heights of the control bodies located at the top and bottom of the frost layer are $\frac{1}{2}dx$, and the other control bodies are high *dx*. The energy and mass equilibrium equations of the frost layer and the incoming air are presented below.

The energy conservation equation for the frost layer can be expressed as:

$$k_{\mathrm{f}}(x)\frac{d^2T_{\mathrm{f}}(x)}{dx^2} = i_{\mathrm{sv}}C\rho_{\mathrm{a}}(x)\left(w_{\mathrm{f}}(x) - w_{\mathrm{sat}}(x)\right)dx \tag{5}$$

C indicates the empirical value of the absorption coefficient of water vapor by the frost layer, and it is expressed in 1/s. The value of C is mainly determined by the structure of the frost layer, and very low values of C lead to unrealistically large values of water vapor density, as C is on the order of 100 or higher [24]. In this work, C is set at 500 to ensure that the calculation results of the frost model and experimental measurement results are consistent.

The mass conservation equation for the frost layer can be expressed as:

$$D_{\mathrm{eff}}(x)\rho_{\mathrm{a}}(x)\frac{d^2w_{\mathrm{f}}(x)}{dx^2} = C\rho_{\mathrm{a}}(x)\left(w_{\mathrm{f}}(x) - w_{\mathrm{sat}}(x)\right)dx \tag{6}$$

The sensible heat transfer between the incoming air and frost layer $Q_{\mathrm{sens.a}}$ can be described as:

$$Q_{\mathrm{sens.a}} = c_{\mathrm{p.a}}m_{\mathrm{a}}(T_{\mathrm{a,in}} - T_{\mathrm{a,out}}) = q_{\mathrm{sens.fs}}A_{\mathrm{fs}} \tag{7}$$

The mass transfer of incoming air and frost layer M_{a} can be expressed as:

$$M_{\mathrm{a}} = m_{\mathrm{a}}(W_{\mathrm{a,in}} - W_{\mathrm{a.out}}) = m_{\mathrm{fs}}A_{\mathrm{fs}} \tag{8}$$

The thermal conductivity of the frost layer k_{f} is related only to the frost density, which is calculated as [25]:

$$k_{\mathrm{f}}(x) = 0.132 + 3.13\times10^{-4}\rho_{\mathrm{f}}(x) + 1.6\times10^{-7}\rho_{\mathrm{f}}(x)^2 \tag{9}$$

The effective water diffusion coefficient D_{eff} in the frost layer is calculated according to the empirical formula proposed by Breque [26], and D_{std} denotes the standard water diffusion coefficient:

$$D_{\mathrm{eff}}(x) = \frac{D_{\mathrm{std}}\left[\rho_{\mathrm{i}} - \rho_{\mathrm{f}}(x)\right]}{\rho_{\mathrm{i}} - 0.58\rho_{\mathrm{f}}(x)} \tag{10}$$

The third boundary condition is adopted for the heat and mass transfer between the incoming air and the frost layer surface. The sensible heat flux $q_{\mathrm{sens.fs}}$ and the water mass flux m_{fs} on the frost layer surface can be calculated as:

$$q_{\mathrm{sens.fs}} = h_{\mathrm{eff}}\left(\overline{T_{\mathrm{a}}} - T_{\mathrm{fs}}\right) \tag{11}$$

$$m_{\mathrm{fs}} = h_{\mathrm{m.eff}}\rho_{\mathrm{a}}\left(\overline{w_{\mathrm{a}}} - w_{\mathrm{fs}}\right) \tag{12}$$

The convective heat transfer coefficient h_{eff} is calculated by the empirical formula with the j factor [27]. The j factor is used to calculate the convective heat transfer coefficient of finned-tube heat exchangers with good accuracy and generality, and j factor formula proposed by McQuiston is applied with an applicability range of 700<Re<5000:

$$h_{\mathrm{eff}} = j_{\mathrm{N}}\rho_{\mathrm{a}}v_{\mathrm{a.max}}c_{\mathrm{p.a}}\,\mathrm{Pr}_{\mathrm{a}}^{-\frac{2}{3}} \tag{13}$$

$$j_{\mathrm{N}} = 0.991 j_4 (2.24\,\mathrm{Re}^{-0.092}\times\left(N/4\right)^{-0.031})^{0.607(N-4)} \tag{14}$$

$$j_4 = 0.0014 + 0.2618\,\mathrm{Re}^{-0.4}\left(\frac{A_{\mathrm{total}}}{A_{\mathrm{tube}}}\right)^{-0.15} \tag{15}$$

$$\mathrm{Re} = \frac{m_{\mathrm{air}}d_{\mathrm{out}}}{A_{\mathrm{min}}\mu_{\mathrm{air}}} \tag{16}$$

The mass transfer coefficient $h_{\mathrm{m,eff}}$ is calculated by the Lewis equation:

$$h_{\text{m.eff}} = \frac{h_{\text{eff}}}{\rho_{\text{a}} c_{\text{p.a}}} L_{\text{e}}^{-\frac{2}{3}} \tag{17}$$

The second boundary condition is applied for the heat transfer between the frost layer and the finned-tube evaporator, and the equivalent temperature of the finned-tube evaporator surface T_{sft} can be calculated as [28] Eq. (18). The average temperature of the incoming air $\overline{T_{\text{a}}}$ takes its arithmetic average of the inlet and outlet temperatures of the finned-tube evaporator.

$$T_{\text{sft}} = \overline{T_{\text{a}}} - \frac{(A_{\text{tube}} + \eta_{\text{fin}} A_{\text{fin}})(\overline{T_{\text{a}}} - T_{\text{tube}})}{A_{\text{fin}} + A_{\text{tube}}} \tag{18}$$

The mass transfer is 0 on the contact surfaces between the frost layer and the finned-tube evaporator:

$$D_{\text{eff}} \rho_{\text{a}} \left. \frac{dw_{\text{f}}}{dx} \right|_{x=0} = 0 \tag{19}$$

The capacity and velocity of incoming air in the finned-tube evaporator are important boundary conditions for solving the frost model. The resistance of the finned-tube evaporator increases because of the growth of the frost on its surface, resulting in changes in the flow rate of the incoming air. The evaporator fan speed also varies under different operating conditions. Therefore, it is necessary to derive the flow rate of the incoming air in the finned-tube evaporator under various fan speeds. The relationship between the full pressure p_{e} and the speed of the fan N_{r} is Eq. (20), and the evaporator fan similar law formula constant C_1 takes 0.1 [29].

$$p_{\text{e}} = C_1 \rho_{\text{a}} N_{\text{r}}^2 \tag{20}$$

The resistance factor f of the finned-tube evaporator is defined as [30]:

$$f = \frac{2\Delta p}{\rho_a v_{a.max} L / d_3} \tag{21}$$

The resistance factor f can also be calculated by the following formula for flat finned-tube evaporators:

$$f = 5.504\,\mathrm{Re}^{-0.454}\left(\frac{s}{d_3}\right)^{-0.940} \tag{22}$$

The flow rate at the narrowest flow path $v_{a.max}$ can be derived by equating the full fan pressure to the total pressure drop of the incoming air along the length of the finned-tube evaporator:

$$v_{a.max} = C_1 \frac{s^{0.608} d_3^{\,0.333}}{L^{0.647} \nu^{0.294}} N_r^{\,1.294} \tag{23}$$

The water mass flux at the surface of the frost layer is composed of two parts, and the part for increasing the frost density can be computed as:

$$m_\rho = D_{eff}\,\rho_a \left.\frac{dw_f}{dx}\right|_{x=fs} \tag{24}$$

Then the part condensing at the contact surface and thickening the frost layer can be expressed as:

$$m_\delta = m_{fs} - m_\rho \tag{25}$$

The thickness of the frost layer at each time step can be formulated as:

$$\delta_f\left(\tau + \Delta\tau\right) = \delta_f\left(\tau\right) + \frac{m_\delta(\tau)\times\Delta\tau}{\left.\rho_f(\tau)\right|_{x=fs}} \tag{26}$$

2.3 Numerical methods

The above boundary conditions were brought into the conservation equations and the diffusion term discretization was in the central difference format. The grid was divided into 100 due to the thin frost layer, and it was found that further increasing the grid number would not affect the calculation results after several tests. The time step should be small enough to improve the accuracy of the quasi-steady-state model, but cannot be too small due to the required computational speed for a large number of computations. So, the time step was set to 5 s after several tests to meet the above requirements. The frost thickness was updated at the end of each time step. The initial conditions required for the frost model include the initial frost thickness and frost density, which were taken as 0.01 mm and 25 kg/m^3 respectively. The parameters to be input are external temperature and moisture content, tube-base temperature of the finned-tube evaporator, evaporator fan speed, and solar irradiance. The model was solved by Python and the physical parameters of air were obtained from the REFPROP. The solution procedure of the frosting model coupled with the TSAC model is shown in Fig. 4.

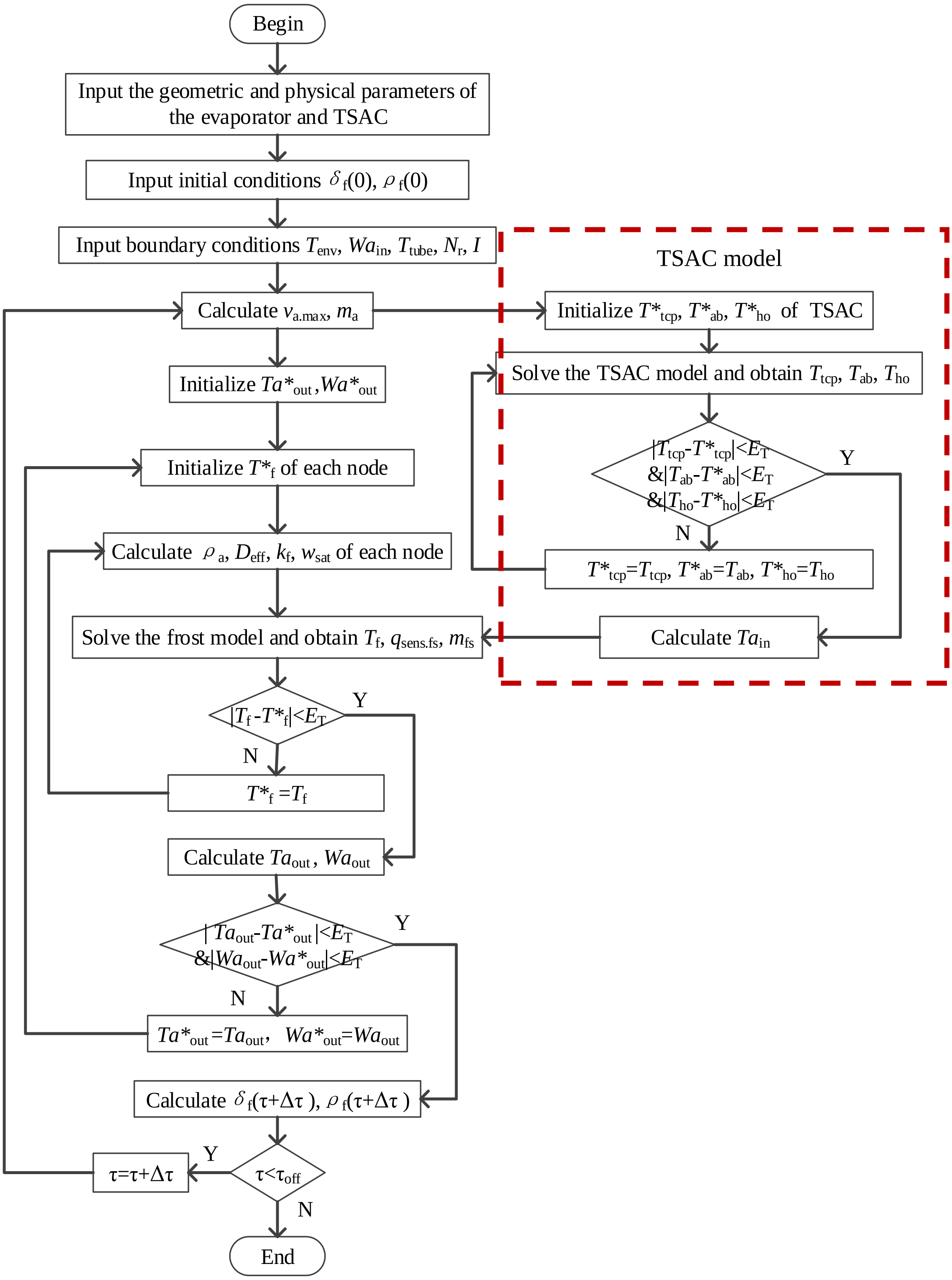

Fig. 4. The solution procedure of the coupled model

And the solution procedure can be expressed as follow:

(1) Use the initial frost layer thickness to calculate the flow rate of air in the evaporator, and input the required boundary conditions into the TSAC model to

calculate the inlet temperature of the incoming air.

(2) Determine the average temperature and moisture content of the incoming air and frost layer heat transfer by making reasonable assumptions about air temperature and moisture content.

(3) Assume the frost layer temperature at each node to calculate the dry air density, effective water vapor diffusion coefficient, frost layer thermal conductivity, and moisture content of saturated wet air.

(4) Solve the node equations to obtain the new frost layer temperature of each node, then return to the previous step to iterate, until the frost layer temperature distribution and heat and mass transfer between the frost layer and the incoming air are reasonable.

(5) Using the equilibrium equation for air, calculate the new incoming air outlet temperature and moisture content, then return to step 2 for iterative calculations to obtain reasonable incoming air outlet parameters.

(6) Update the frost thickness and density.

(7) Return to step 1 and enter the new frost thickness for the next time step, repeating this process until the frost thickness reaches the upper limit.

3 Results and discussion

3.1 Model validation

The heat transfer model of TSAC has been verified in the previous study [23], and the frost model of the finned-tube evaporator is validated by the experimental data of Zhang et al [6]. The frost thickness distribution was determined by taking high-resolution camera shots of the frosted surface on the finned-tube evaporator every 5 minutes and the measurement uncertainty was ±2.53%. The geometric parameters of the finned-tube evaporator and the experimental frosting conditions are shown in Table 2.

Table 2. The geometric parameters of the evaporator and the experimental frosting conditions.

Geometric parameters of the evaporator	Frosting conditions
Length×width×height: 243×150×22 (mm×mm×mm)	Frosting cycle: 3600s
Rib thickness: 2mm; tube outer diameter: 9.52mm	Tube base temperature: -10 ℃
Rib spacing: 0.2mm; tube spacing: 25mm	Income air temperature: 2 ℃
Number of ribs: 76; number of tube rows: 1	Income air moisture content: 3.74 g/kg

Fig. 5 illustrates the calculated and measured values of the frost thickness and the incoming airflow with the frosting process. As the frost grew, the pressure drop of the incoming air along the finned-tube evaporator increased, and the incoming air flow rate was reduced from 150 m^3/h to 40 m^3/h at a constant fan speed in the experiment. The calculated values of incoming airflow were slightly smaller than the experimental test values with an average relative error of 9.9 % at a fan speed of 353 rpm. The measured frost thickness on the surface of the finned-tube evaporator is divided into two types: the frost thickness on the windward side (front) and the leeward side (back). The windward side frost was significantly thicker than the leeward side in the early stage of frosting, while the two gradually converged later. The average relative error between the experimentally measured frost thickness and the model calculated value was 12.3 %. The error mainly occurred before 1200 s of frosting because of the large difference in frost thickness between the front and back of the finned-tube evaporator, which was contrary to the assumption of uniform frost distribution over the effective frosting area in the frosting model. At the later stage of frosting, the distribution of frost thickness tended to be uniform, and the error between the measured and calculated values gradually decreased. After 1200 s, the relative error was only 8.9%. The frost layer was thin at the early stage of frosting, and the average frost thickness measured at 1200 s was only 0.6 mm. The thermal resistance of the frost layer is very small, which has less impact on the performance of heat pump systems, so the accuracy of the model prediction is more important in the late frost period. In summary, there is reasonable agreement between the experimental test values and the model predictions of the frost thickness, indicating that the frosting model developed in this paper is reliable.

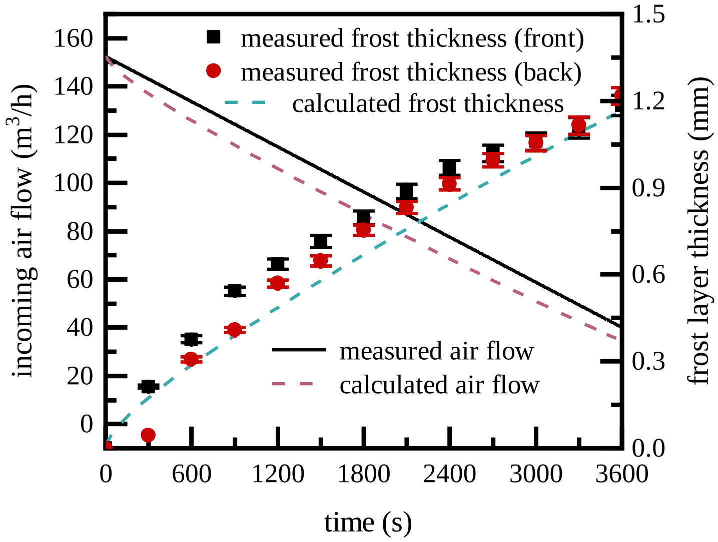

Fig. 5. Comparison of calculated and measured values of frost thickness

3.2 Frosting situation comparison at different moments

The key parameters affecting the frost condition of the ASHP include the environment temperature and moisture content, the tube base temperature of the finned-tube evaporator, and the solar irradiance. In this section, the installed area of the TSAC was 2 m^2 and the evaporator fan speed was fixed at 500 rpm. Since the finned-tube gap of the evaporator was 1.17 mm, the frost thickness was limited to 0.58 mm. The standard values of each key parameter were: environment temperature of 2 °C, ambient air moisture content of 3.4 g/kg, tube base temperature of - 10 °C and solar irradiance of 300 W/m^2.

Fig. 6 demonstrates the comparison of the frosting situation between the ASHP with the TSAC (TSAHP) and the conventional ASHP at different moments. As illustrated in Fig. 6 (a), the sensible and latent heat fluxes between the incoming air and the frost surface decreased as frosting proceeded. This is due to two reasons, on the one hand, larger thermal resistance leads to a higher temperature and saturated air moisture content on the frost layer surface, and a lower flow rate makes smaller average temperature and moisture content of the incoming air. As a result, the temperature and moisture content difference between the incoming air and the frost layer surface decreases. On the other hand, the reduced flow rate lessens the convective heat and mass transfer coefficient between the incoming air and the frost layer surface. The sensible heat flux was higher than the latent heat flux throughout the frosting process, but the sensible heat flux declined more quickly. The difference between sensible and latent heat fluxes for the TSAHP dropped from 168.2 W/m^2 to 124.2 W/m^2 from the beginning of frosting to 1800 s.

The total and sensible heat fluxes between the incoming air and the frost surface were higher for TSAHP than for ASHP, attributed to the greater temperature difference between the frost surface and the air preheated by the TSAC before entering the evaporator of the TSAHP. As shown in Figure 6 (c), the frost thickness of ASHP increased at a smaller rate and the flow rate of incoming air decreased more slowly as the frosting progressed, hence the sensible and latent heat fluxes decreased more slowly. The total heat flux of TSAHP was 21.8 W/m^2 higher than that of ASHP at the beginning of frosting, and 101.4 W/m^2 higher at the 1800 s of frosting.

As indicated in Fig. 6 (b), the trends of water vapor diffusion flux were similar to those of heat flux, but with a minor difference between TSAHP and ASHP. Since the surface temperature and the corresponding saturated moisture content of the TSAHP frost layer are higher, the moisture content difference with the incoming air is smaller. Thus, the water vapor diffusion flux used to increase the frost thickness of TSAHP is less than that of ASHP at the early stage of frosting. At the same time, the water vapor diffusion flux to increase the density was greater due to the larger temperature gradient and larger saturated air moisture content gradient in the frost layer of the TSAHP. In summary, the frost thickness of TSAHP was smaller due to the lower water vapor diffusion flux for increasing the frost thickness and higher water vapor diffusion flux for increasing the frost density. In this paper, the tube base temperature was fixed to explore the effects of a single variable. In real system operation, the evaporation temperature and tube base temperature of TSAHP are higher than those of traditional ASHP, which further reduces the frosting of TSAHP. The water vapor diffusion fluxes of both systems are primarily used to increase frost thickness. For TSAHP, the water vapor diffusion flux for thickening frost layer was 2.5 times greater than that for increasing frost density throughout the frosting process.

The difference in frost thickness for TSAHP and ASHP during the frosting process is depicted in Fig. 6 (c). The frost thickness gradually rose in the frosting process, but its development rate slowed due to the lower water vapor diffusion flux between the incoming air and the frost layer surface. The growth rates of TSAHP and ASHP frost thickness fell 36.7 % and 38.3 %, respectively, from the beginning of frosting until the 1800s. The frost of TASHP grew slower than ASHP, and TSAHP frost thickness dropped by 9.6% compared to ASHP at 1200 s.

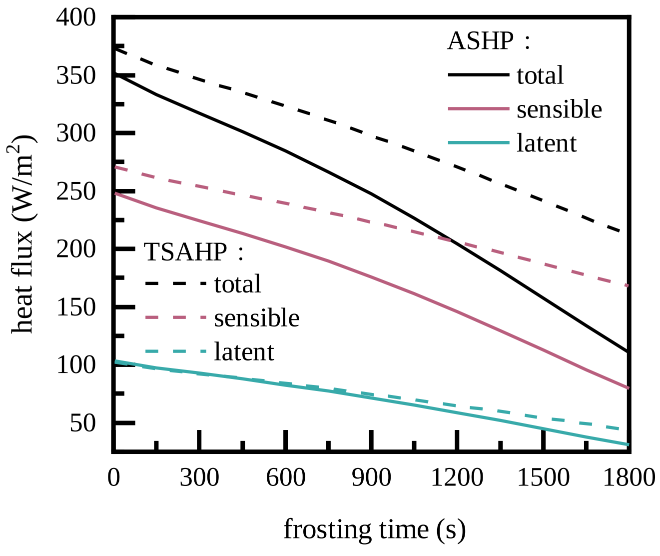

(a)

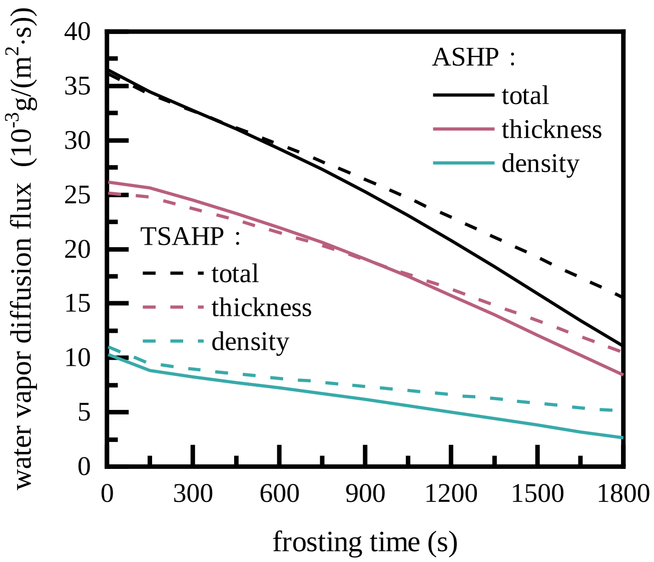

(b)

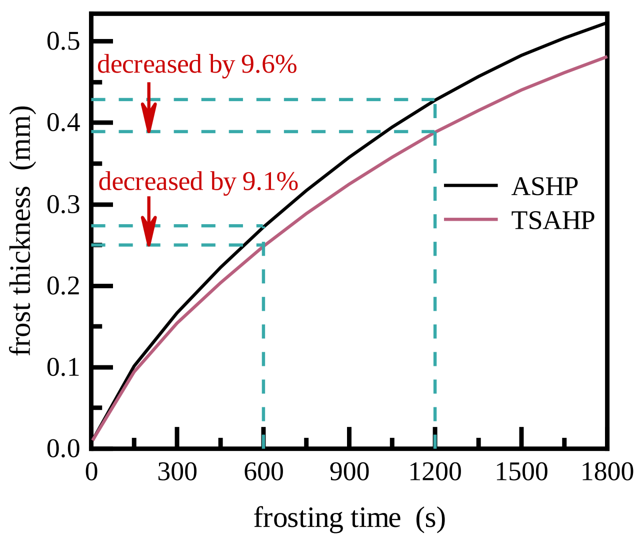

(c)

Fig. 6. The variation of (a) heat flux, (b) water vapor diffusion flux and (c) frost thickness with frost duration

Figure 7 (a) shows the heat fluxes of TSAHP and ASHP at different locations along the frost thickness direction. The heat transfer direction within the frost layer is from the surface to the bottom. The heat flux at the frost layer's surface consists of sensible and latent heat exchange. The sensible heat exchange is between the frost layer's surface and the incoming air. The latent heat exchange from condensing water vapor raises the thickness of the frost layer. During the heat transfer process, the water vapor that increased the frost density condensed and released latent heat of vaporizing, which increased the heat flux. But the heat flux changed less across the entire frost thickness because the condensation heat was minor. Furthermore, the heat flux of TSAHP was greater than ASHP, indicating that the TSAHP evaporator exchanges heat with the incoming air better and has superior system performance throughout the frosting process.

Figure 7 (b) depicts the water vapor diffusion fluxes of TSAHP and ASHP at various positions along the frost thickness direction. The water vapor diffusion flux was the greatest on the frost surface, and the water vapor is continuously absorbed by the frost layer as it spread from the frost surface to the bottom. The water vapor diffusion flux gradually decreased and it was 0 kg/(m^2·s) at the interface between the frost layer and the finned-tube evaporator. Furthermore, as frosting progressed, the frost layer density increased, and the water vapor diffusion flux and the amount of water vapor entering the frost layer decreased, resulting in the smallest gradient of water vapor diffusion flux at the 1800s. Similarly, the water vapor diffusion fluxes of TSAHP and ASHP followed a similar decreasing trend, with TSAHP having slightly higher values.

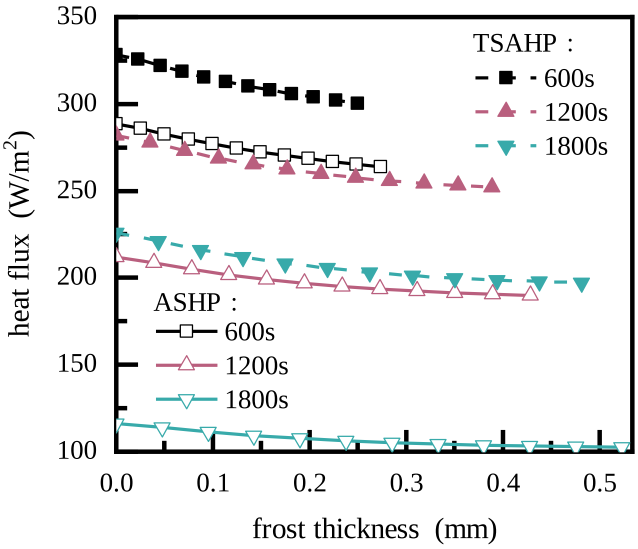

(a)

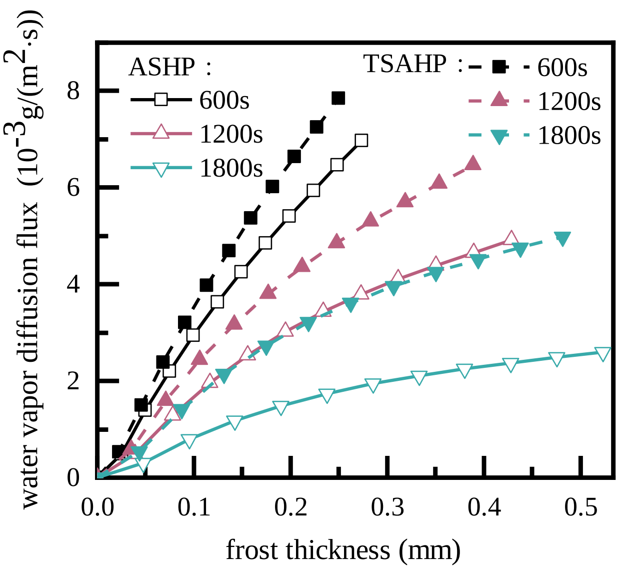

(b)

Fig. 7. (a) Heat fluxes and (b) water vapor diffusion fluxes at various frost thicknesses

3.3 Frosting situation comparison at different operating conditions

In this section, when analyzing the influence of a parameter, the values of the other parameters were set to be constant in accordance with the standard values. The standard values for each key parameter were 2 °C environment temperature, 3.4 g/kg ambient air moisture content, - 10 °C tube base temperature, and 300 W/m^2 solar irradiance.

Fig. 8 compares the frost thickness of TSAHP and ASHP at three moments under different ambient temperatures. The temperature of incoming air rise along with the ambient temperature, leading to the increase of the frost layer surface's temperature and its saturated moisture content. And then the water vapor diffusion flux between the incoming air and the frost layer surface falls. Furthermore, as the finned-tube evaporator's equivalent temperature and frost layer temperature increase, the diffusion coefficient between the frost and the wet air inside it rises, raising the water vapor diffusion flux for increasing the frost density. Frost thickness decreases due to the interaction of decreasing total water vapor diffusion flux and increasing water vapor diffusion flux for enlarging frost density. As the ambient temperature rose from -2 °C to 6 °C, the TSAHP frost thickness decreased by 0.11 mm, 0.17 mm, and 0.22 mm at 600 s, 1200 s, and 1800 s, respectively. The frost thickness decreased more at later frosting moments as higher ambient temperatures could consistently restrain the growth of frost. Compared with the ASHP, the rate of frost thickness reduction at different moments was slightly slower for TSAHP, as the TSAC had a greater impact on the preheating of incoming air at lower ambient temperatures. Above all, the benefit of TSAHP in postponing frost is greater with lower ambient temperature and longer frost cycles.

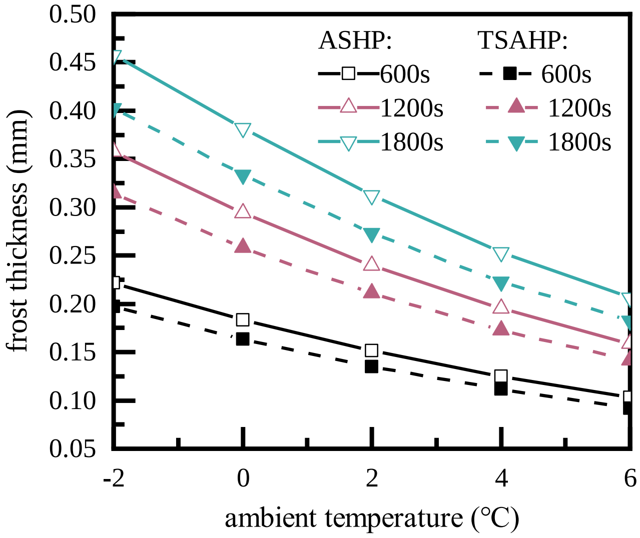

Fig. 8. The frost thickness of TSAHP and ASHP at different ambient temperatures

Fig. 9 compares the frost thicknesses of TSAHP and ASHP at three moments with various incoming air moisture contents. As the moisture content of the incoming air increased, the thickness of the frost layer increased linearly at all frosting moments, and the frost thickness of TSAHP was thinner than that of ASHP. The average frost thickness of TSAHP was 10.4% less than ASHP at all air moisture content. At later stages of frosting, increasing the incoming air moisture content had less impact on the growth of the frost thickness, as the frost thickness and the saturated air moisture content corresponding to the frost surface temperature increased, resulting in a decrease in the amount of incoming air and the water vapor diffusion flux between the incoming air and the frost surface.

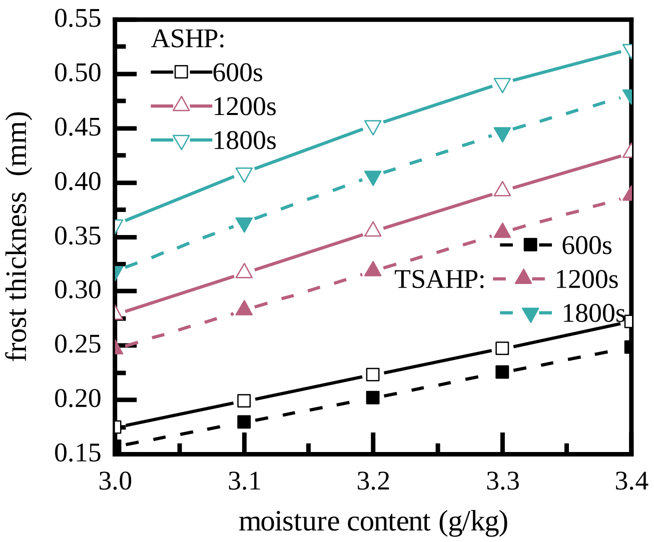

Fig. 9. The frost thickness of TSAHP and ASHP with different incoming air moisture content

Fig. 10 compares the frost thicknesses of TSAHP and ASHP at three different moments for various tube base temperatures of the finned-tube evaporator. With the tube base temperature increased, the equivalent temperature of the finned-tube evaporator was higher, the frost layer temperature went up. The higher frost surface temperature led to the larger saturated air moisture content, as the water vapor diffusion flux between the incoming air and the surface of the frost layer, and the thickness of the frost layer decreased. When the tube base temperature was -14 °C, the frost thickness of TSAHP increased by 0.24 mm from 600 s to 1800 s, but when the tube base temperature was -6 °C, it only increased by 0.02mm. Both TSAHP and ASHP experienced the same trend in frost thickness as the tube base temperature rose. At 1800 s, the frost thickness decreased by 0.45 mm for TSAHP and 0.47 mm for ASHP as the tube base temperature increased from -14 ℃ to -6 ° C.

The frost thickness can be reduced by increasing both the tube base temperature and the ambient temperature, but the tube base temperature had a greater effect. It was due to the tube base temperature having a greater impact on the equivalent temperature of the finned-tube evaporator surface, which in turn had a greater impact on the frost layer temperature distribution and saturated air moisture content of the saturated air on the frost layer surface, as well as the water vapor diffusion flux between the incoming air and frost layer surface. At the 1800s, the frost thickness of TSAHP and ASHP decreased by 9.8% and 9.9% for every 1 °C increase in ambient temperature, while decreased by 27.3% and 25.3% for every 1 °C increase in tube base temperature.

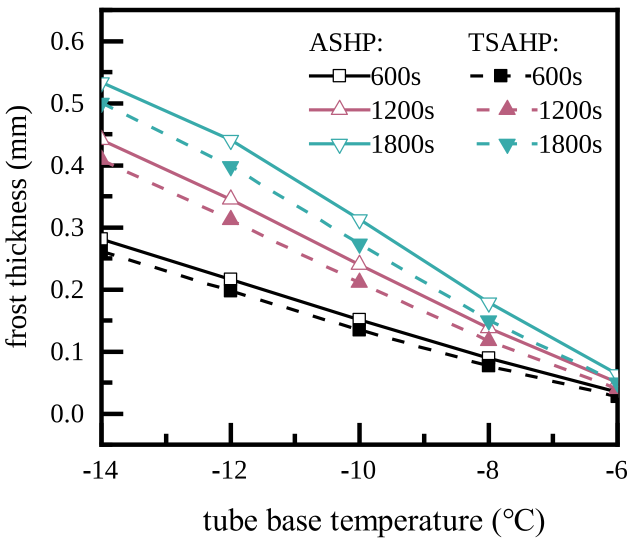

Fig. 10. The frost thickness of TSAHP and ASHP with different tube base temperature

Fig. 11 shows the comparison of the frost thickness of TSAHP and ASHP at three moments with different solar irradiance. The maximum solar irradiance was set at 500 W/m^2, because frosting occurred typically in the early morning when the ambient temperature was low and the moisture content was high. With the solar irradiance increased from 100 W/m^2 to 500 W/m^2, the frost thickness of TSAHP decreased by 12.2 %. The solar irradiance did not affect the thickness of the ASHP frost layer. When the solar irradiance was 500 W/m^2, the average frost thickness of TSAHP at the three moments could be 15.1% less than that of ASHP.

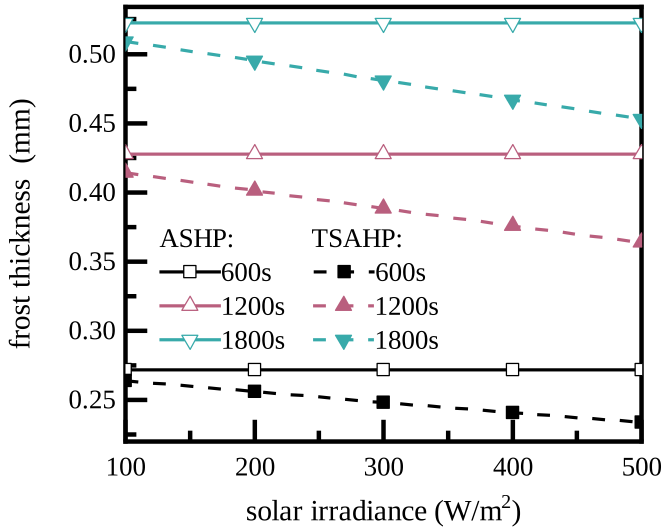

Fig. 11. The frost thickness of TSAHP and ASHP at different solar irradiance

Fig. 13 depicts the frost thickness and evaporator heat exchange capacity of ASHP and TSAHP operating from 9:00 to 17:00 on a typical daily meteorological parameter (Fig. 12) in Dalian, China. The frost thickness was set to zero when the frost filled the finned-tube gap, symbolizing the defrosting of the system. And both the frost thickness and heat exchange capacity varied periodically and the nodes of abrupt changes corresponded to each other. The frost thickness growth rate of TSAHP was significantly slower than that of ASHP, and TSAHP defrosted twice less than ASHP during the eight-hour daytime period. This was due to increases in direct solar irradiance and ambient temperature, both of which help the TSAC preheat the incoming air and raise the evaporating temperature, then slowed the growth of frost thickness.

When the frost thickness went up, the evaporator heat exchange of the ASHP decreased, and that of the TSAHP continued to grow. The thicker frost layer enhanced the convective heat exchange thermal resistance of the evaporator surface, causing the convective heat exchange between the incoming air and the finned-tube evaporator to be weak. However, because TSAHP used TSAC to preheat the incoming air, and the heat collection of TSAC became stronger as the direct solar radiation increased, the temperature of the incoming air sweeping through the evaporator rose. As a result, the temperature difference between the incoming air and the evaporator surface was greater and the heat transfer was stronger, so the heat exchange of the evaporator in TSAHP stayed growing as the frost thickened during a frost process. During the eight hours of daylight, the total heat exchange of the TSAHP evaporator was 36.6% greater than that of the ASHP.

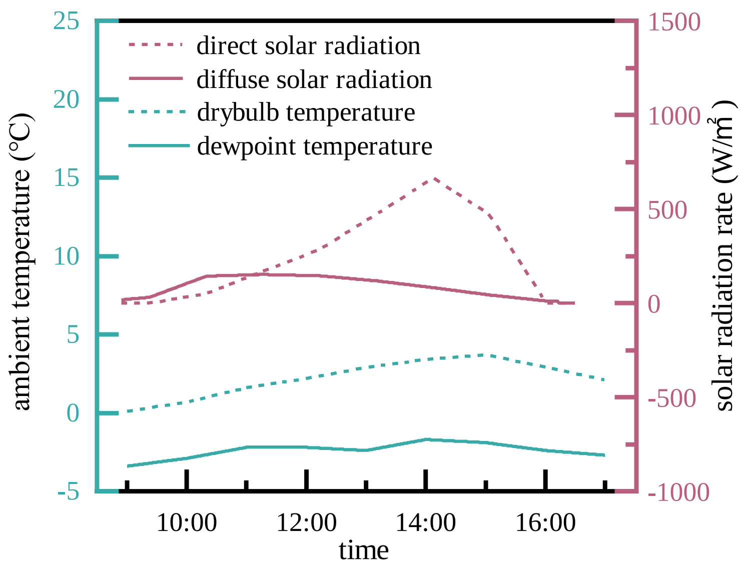

Fig. 12. The typical daily meteorological parameters in Dalian, China

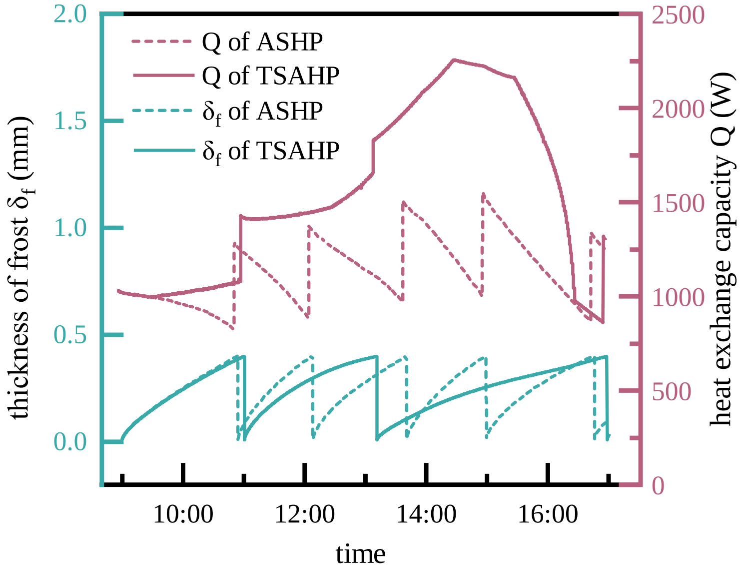

Fig. 13. The frost thickness and evaporator heat transfer capacity of TSAHP and ASHP on a typical day

4 Conclusions

In this paper, the triangular solar air collector (TSAC) is adopted for frost restraint of air source heat pump (ASHP). The dynamic heat transfer model of the TSAC and a quasi-steady-state frosting model of the ASHP were established and coupled. The correlation equation between frost layer thickness and evaporator air flow is derived to make the coupled model better applicable. The frosting characteristics of the ASHP with the TSAC (TSAHP) and the conventional ASHP were compared and analyzed. The main conclusions can be drawn as follows.

(1) The frost model considers the effect of frost thickness variation on incoming air flow, and the average relative error between calculated and tested incoming air flow is 9.9%. The relative error between the calculated and tested frost thickness is 8.9% after uniform frost distribution, indicating the reliability of the frosting model.

(2) The sensible heat flux of incoming air and frost surface is greater than the

latent heat flux, and the water vapor diffusion flux of increasing frost thickness is greater than that of increasing frost density, and the former is 2.5 times the latter for TSAHP.

(3) The frost thickness decreases as the ambient temperature and tube base temperature rise, and the influence of tube base temperature is greater. The frost thickness of TSAHP is 15.1% less than ASHP when the solar irradiance is 500 W/m^2.

(4) The TSAHP increases the heat flux by 36.6% and reduces half of the defrosting times compared with the conventional ASHP under standard operating conditions, indicating that the TSAC is effective in restraining the frosting of ASHP, which helps ASHP operate efficiently.

Acknowledgments

The authors are grateful for the financial support provided by the China National Key R&D Program [Grant No.2020YFD1100305-02].

References

[1] Zhang H, Zhao X, Zhang R., Synergistic development of heating system decarbonization transition and large-scale renewable energy penetration: A case study of Beijing, Energy Conversion and Management 269 (2022) 116142. https://doi.org/10.1016/j.enconman.2022.116142

[2] Ermel C., Marcus V.A. Bianchi, A. P. Cardoso, et al., Thermal storage integrated into air-source heat pumps to leverage building electrification: A systematic

literature review, Applied Thermal Engineering 215 (2022), 118975. https://doi.org/10.1016/j.applthermaleng.2022.118975

[3] Zheng Z, Zhou J, Xu F, et al., Solar assisted air source heat pump systems for campus water heating in China: Economic optimization of solar fraction design, Applied Thermal Engineering 213 (2022), 118767. https://doi.org/10.1016/j.applthermaleng.2022.118767

[4] Carroll P, Chesser M, Lyons P., Air Source Heat Pumps field studies: A systematic literature review, Renewable and Sustainable Energy Reviews 134 (2020), 110275. https://doi.org/10.1016/j.rser.2020.110275

[5] Yao Y, Jiang Y, Deng S, et al., A study on the performance of the airside heat exchanger under frosting in an air source heat pump water heater/chiller unit, International Journal of Heat and Mass Transfer 47 (2004) 3745-3756. https://doi.org/10.1016/j.ijheatmasstransfer.2004.03.013

[6] Wang Z, Song M, Wang F, et al., Experimental investigation and seasonal performance assessment of a frost-free ASHP system with radiant floor heating, Energy and Buildings 179 (2018) 200-212. https://doi.org/10.1016/j.enbuild.2018.09.019

[7] Fan Y, Zhao X, Han Z, et al., Scientific and technological progress and future perspectives of the solar assisted heat pump (SAHP) system, Energy 229 (2021), 120719. https://doi.org/10.1016/j.energy.2021.120719

[8] Mengjie S, Chaobin D, Shengchun L, et al., Frost layer thickness measurement and calculation: a short review, Energy Procedia 142 (2017) 3812-3819.

https://doi.org/10.1016/j.egypro.2017.12.281

[9] Zhang L, Song M, Mao N, et al., Temporal and spatial frost growth prediction of a tube-finned heat exchanger considering frost distribution characteristics, International Journal of Heat and Mass Transfer 183 (2022), 122192. https://doi.org/10.1016/j.ijheatmasstransfer.2021.122192

[10] Zhang L, Jiang Y, Dong J, et al., An experimental study on the effects of frosting conditions on frost distribution and growth on finned tube heat exchangers, International Journal of Heat and Mass Transfer 128 (2019) 748-761. https://doi.org/10.1016/j.ijheatmasstransfer.2018.09.016

[11] Seker D, Karatas H, Egrican N., Frost formation on fin-and-tube heat exchangers. Part I—Modeling of frost formation on fin-and-tube heat exchangers, International Journal of Refrigeration 27 (2004) 367-374. https://doi.org/10.1016/j.ijrefrig.2003.12.003

[12] Ji W, Cai J, Ji J, et al., Experimental study of a direct expansion solar-assisted heat pump (DX-SAHP) with finned-tube evaporator and comparison with conventional DX-SAHP, Energy and Buildings 207 (2020), 109632. https://doi.org/10.1016/j.enbuild.2019.109632

[13] M.S. Patil, J.H. Seo, M.Y. Lee., Heat transfer characteristics of the heat exchangers for refrigeration, air conditioning and heat pump systems under frosting, defrosting and dry/wet conditions—A review, Applied Thermal Engineering 113 (2017) 1071-1087. https://doi.org/10.1016/j.applthermaleng.2016.11.107

[14] Song M, Deng S, Dang C, et al. Review on improvement for air source heat pump units during frosting and defrosting, Applied Energy 211 (2018) 1150-1170. https://doi.org/10.1016/j.apenergy.2017.12.022

[15] Tan H, Xu G, Tao T, et al. Experimental investigation on the defrosting performance of a finned-tube evaporator using intermittent ultrasonic vibration, Applied Energy 158 (2015) 220-232. https://doi.org/10.1016/j.apenergy.2015.08.072

[16] Sonobe N, Fukiba K, Sato S, et al. Method for defrosting heat exchangers using an air-particle jet, International Journal of Refrigeration 60 (2015) 261-269. https://doi.org/10.1016/j.ijrefrig.2015.08.017

[17] Lee M, Kim Y, Lee H, et al. Air-side heat transfer characteristics of flat plate finned-tube heat exchangers with large fin pitches under frosting conditions, International Journal of Heat and Mass Transfer 53 (2010) 2655-2661. https://doi.org/10.1016/j.ijheatmasstransfer.2010.02.047

[18] Huang W, Zhang T, Ji J, et al. Numerical study and experimental validation of a direct-expansion solar-assisted heat pump for space heating under frosting conditions, Energy and Buildings 185 (2019) 224-238. https://doi.org/10.1016/j.enbuild.2018.12.033

[19] Kong X, Li J, Wang B, et al. Numerical study of a direct-expansion solar-assisted heat pump water heater under frosting conditions based on experiments, Solar Energy 196 (2020) 10-21. https://doi.org/10.1016/j.solener.2019.11.104

[20] Dong Z, Chang L, Jianjun Z, et al. Thermal economic analysis of a double-channel solar air collector coupled with draught fan: Based on energy grade, Renewable Energy 170 (2021) 936-47. https://doi.org/10.1016/j.renene.2021.02.051

[21] Hu J, Liu K, Ma L, et al. Parameter optimization of solar air collectors with holes on baffle and analysis of flow and heat transfer characteristics, Solar Energy 174 (2018) 878-87. https://doi.org/10.1016/j.solener.2018.09.075

[22] Saini P, Paolo B, Fiedler F, et al., Techno-economic analysis of an exhaust air heat pump system assisted by unglazed transpired solar collectors in a Swedish residential cluster, Solar Energy 224 (2021) 966-983. https://doi.org/10.1016/j.solener.2021.06.026

[23] Jiang Y, Zhang H, Wang Y, et al. A comparative study on the performance of a novel triangular solar air collector with tilted transparent cover plate, Solar Energy 227 (2021) 224-235. https://doi.org/10.1016/j.solener.2021.08.083

[24] El Cheikh A, Jacobi A. A mathematical model for frost growth and densification on flat surfaces, International Journal of Heat and Mass Transfer 77 (2014) 604-11. https://doi.org/10.1016/j.ijheatmasstransfer.2014.05.054

[25] Lee K-S, Kim W-S, Lee T-H. A one-dimensional model for frost formation on a cold flat surface, International Journal of Heat and Mass Transfer 40 (1997)

4359-65.
https://doi.org/10.1016/S0017-9310(97)00074-4
[26] Breque F, Nemer M. Modeling of a fan-supplied flat-tube heat exchanger exposed to non-uniform frost growth, International Journal of Refrigeration 75 (2017) 129-40.
https://doi.org/10.1016/j.ijrefrig.2016.12.012
[27] Gray D L, Webb R L. Heat transfer and friction correlations for plate finned-tube heat exchangers having plain fins, International Heat Transfer Conference 8, August, 17-22, 1986, San Francisco, USA.
https://doi.org/10.1615/IHTC8.1200
[28] Yang S, Tao W. Heat Transfer, Beijing: Higher Education Press, 2006.
[29] Cai Z, Long T. Hydrodynamic Pumps and Fans, Beijing: China Architecture & Building Press, 1999.
[30] Li W, Tao W, Kang H, et al. EXPERIMENTAL STUDY ON HEAT TRANSFER AND PRESSURE DROP CHARACTERISTICS FOR FIN–AND-TUBE HEAT EXCHANGERS, CHINESE JOURNAL OF MECHANICAL ENGINEERING 33 (1997) 81-86.